Electronic Supplementary Material (ESI) for Chemical Science.
This journal is © The Royal Society of Chemistry

Supporting Information

Selectivity descriptors of the catalytic *n*-hexane cracking process over 10-membered ring zeolites

Pandong Ma [a], Hexun Zhou [a], Yubing Li [b], Mengheng Wang [b], Stefan Adrian F. Nastase [c], Mengsi Zhu [d], Jiale Cui [b], Luigi Cavallo [c], Kang Cheng [b, *] and Abhishek Dutta Chowdhury [a, *]

[a] College of Chemistry and Molecular Sciences, Wuhan University, Wuhan 430072 Hubei, PR China
[b] State Key Laboratory of Physical Chemistry of Solid Surfaces, Collaborative Innovation Center of Chemistry for Energy Materials, College of Chemistry and Chemical Engineering, Xiamen University, Xiamen 361005, PR China
[c] KAUST Catalysis Center (KCC), King Abdullah University of Science and Technology (KAUST), Thuwal 23955, Saudi Arabia
[d] Innovation Laboratory for Sciences and Technologies of Energy Materials of Fujian Province (IKKEM), Xiamen 361005, PR China.

Corresponding Author: abhishek@whu.edu.cn , kangcheng@xmu.edu.cn

S1. Experimental section

S1.1 Materials

ZSM-5 (H type, SAR = 38) zeolite, MCM-22 (H type, SAR = 30) zeolite, and ZSM-22 (H type, SAR = 42) zeolite were purchased from Nankai University Catalyst Co. Ltd. Ferrierite (Ammonium type, SAR = 20) zeolite was purchased from Alfa Aesar (China) Chemical Co. Ltd. The purchased commercial zeolites were directly used after being calcined at 823 K for 6 h in a muffle furnace under air atmosphere. N-hexane (CAS No.: 110-54-3) and hexane-1-^{13}C (CAS No.: 27581-27-7) were purchased from Sigma-Aldrich (Shanghai) Trading Co. Ltd. Nano ZSM-5 zeolite (H type, SAR = 25~35) was purchased from Dalian University of Technology Qiwangda Chemical Technology Co., Ltd.

S1.2 Characterizations

Powder X-ray diffraction (XRD) patterns of all materials were collected in the 2θ angle range of 5-50° on a PANanalytical X'Pert Pro diffractometer equipped with a Johansson monochromator set up for Cu Kα1 radiation (λ = 1.540 Å). The scanning speed is 0.5 °/min. N_2 physisorption measurements at 77 K were performed on a Micromeritics Tristar 3000 Surface Area Analyzer. The element content of the catalysts was determined using inductively coupled plasma optical emission spectroscopy (ICP-OES), in which all samples were dissolved in aqua regia at 353 K for 2 h for the tests. Pyridine-Fourier transform infrared (Py-FTIR) experiment was conducted in the in-situ transient platform CRCP-7070-B (Tianjin Xianquan Company Ltd., PR China), equipped with a Bruker TENSOR II Fourier transform infrared spectrometer. The samples were put into the cell and pretreated at 823 K under vacuum for 1 h to remove impurities. After cooling to room temperature, the cell was scanned, and obtained data were used as background. Then pyridine was adsorbed at room temperature to reach equilibrium. Then the cell was vacuumed for 30 min to remove excess pyridine. The desorption spectrum was obtained by scanning IR when the cell was heated at 423 K. Spectra were recorded in the 1400-1700 cm^{-1} range at a resolution of 4 cm^{-1} and co-addition of 64 scans. The following formulas were used to quantify the Brønsted acid sites (BAS) and Lewis acid sites (LAS):

$$C_{BAS} = 1.88 \times I_B \times R^2/W$$

$$C_{LAS} = 1.42 \times I_L \times R^2/W$$

where I_B and I_L are the integrated absorbance of BAS and LAS, respectively. R is the radius of the catalyst disk (cm), and W is the mass of the catalyst (mg).[1,2] Scanning electron microscopy (SEM) measurements were performed on a Hitachi S-4800 operated at 15 kV. Subsequently, transmission electron microscopy (TEM) measurements were carried out on a Phillips Analytical FEI Tecnai20 electron microscope operated at an acceleration voltage of 200 kV. Solid-state NMR experiments were performed on a Bruker AVANCE NEO 600 MHz using a 3.2 mm H/X/Y three resonance probe testing, ^{27}Al frequency 156.45 MHz, single pulse excitation, cycle delay 1s, an excitation pulse width (30 °) is 0.6 us, rotational speed 15 kHz, using the chemical shift at 0 ppm of $AlCl_3$ solid sample as a reference. The suboptimal conversion levels observed across all zeolites enable a direct comparison of hydrocarbon

selectivity for the purpose of mechanistic investigation by *operando* and solid-state NMR spectroscopy, particularly considering the consistent and stable performance of all effluent hydrocarbon products throughout the reaction. All ^{13}C-related (both 1D and 2D) experiments were performed on Bruker AVANCE NEO 600MHz spectrometers with a conventional double resonance 3.2 mm HX probe. All solid-state NMR measurements were performed at room temperature (298 K) and MAS frequency of 10 kHz (2D experiments) or 16 kHz (1D experiments). Note that effective sample temperatures can be 5-10 degrees higher due to frictional heating. The 1D ^{1}H-^{13}C cross-polarization (CP) spectrums were recorded using a 4 s recycle delay, a 50 ms acquisition time, and an accumulation of 10 k scans. The 2D ^{1}H-^{13}C HETCOR spectrums were using a 3 s recycle delay, 50 ms (F_2) and 2 ms (F_1) acquisition time, and an accumulation of 64 scans. The contact time of ^{1}H-^{13}C heteronuclear correlation (HETCOR) was set to 200 μs to obtain intermolecular interaction. ^{13}C and ^{1}H chemical shifts were referenced externally to adamantane. The preparation process of NMR samples labeled with isotopes is similar to the testing process of UV-vis DRS mentioned below, with the difference being that the raw material used is hexane-1-^{13}C (CAS No. 27581-27-7). Around 10 min of reaction was performed at 803 K for this purpose. The UV-vis diffuse reflectance spectroscopy (UV-vis DRS) measurements were performed with an AvaSpec-ULS2048L-USB2-UA-RS micro-spectrophotometer from Avantes. Halogen and deuterium lamps were used together for illumination. The *in-situ* studies were performed using a Linkam cell (THMS600) equipped with a temperature controller (Linkam TMS94), and its lid was equipped with a quartz window compatible with UV-vis detection, which was further connected to a water cooler. The inlet of the cell was connected to the N_2 gas line. *Operando* UV-vis DRS reactions were performed using ca. 40 mg of the fresh catalyst material without pressing and sieving. Before the experiment, the sample was pretreated *in-situ* at 823 K for 30 min in N_2 (20 mL/min) atmosphere, and then cooled to 803 K. During the experiment, N_2 introduced *n*-hexane into the reaction cell through a bubbler equipped with *n*-hexane. Use AvaSoft 8.11 software to record spectral data within 20 min after the reaction begins. Each UV-vis spectra were collected with 300 accumulations of 50 ms exposure time each. Finally, the reaction was quenched by rapidly cooling the Linkam cell using a Linkam TMS94 temperature controller. The online gas phase product analyses were performed by Pfeiffer OmniStar GSD 350 O3 (1-200 amu) mass spectrometer, which was directly connected to the outlet of the Linkam cell. The National Institute of Standards and Technology (NIST) mass spectrometry database was consulted for assignment and referencing purposes. Herein, Herein, the signals identified at 2 amu, 15 amu, 26 amu, 41 amu, 56 amu, and 91 amu were attributed to hydrogen, methane, ethylene, propylene, butene, and toluene, respectively. *Operando* experiments were conducted using two distinct approaches: one involved a flow, as discussed earlier, while in the other approach, the liquid was chemisorbed on solid zeolites, followed by temperature-programmed gradual heating. In both cases, a Linkam cell was connected to a mass spectrometer.

S1.3 DFT calculation methods

Geometry optimizations. Periodic DFT calculations were conducted using the Vienna ab initio Simulation Package (VASP) [3,4] , the Perdew−Burke−Ernzerhof functional [5] with Grimme's

dispersion correction [6] (PBE-D3), and a plane-wave basis set of the projector-augmented-wave (PAW) method. [7] An energy cut-off of 600 eV was used for the expansion of the wave function in the plane wave basis set. A (1 × 1 × 1) γ-centered k-point mesh was employed to sample the first Brillouin zone and Gaussian smearing with a width of 0.5 eV. All atoms were relaxed until electronic energies varied by < 1×10^{-5} eV, and the forces on all atoms were < 0.01 eV $Å^{-1}$. This method has been successfully employed previously to simulate zeolite adsorbate models, [8,9] with comparable results to QM/MM cluster simulations. [10,11] The acid sites of interest were chosen based on their similar symmetry. To probe the effect of the sinusoidal channel and intersection, the T8 and T12 sites were substituted with Al, with the corresponding charge-neutralizing H atom used as the Brønsted acid site.

S1.4 Catalytic assessment

The catalytic performances were evaluated on a normal pressure fixed-bed reactor built by Xiamen Hande Engineering Co., Ltd. An HPLC pump was used to inject the *n*-hexane feed (0.02 mL/min), which was vaporized at 423 K and mixed with N_2 (40 mL/min). Typically, a 0.2 g catalyst with sieved sizes of 250-600 μm (30-60 meshes) was loaded in a stainless-steel reactor (inner diameter is 8 mm), and the remaining volume of the reactor tube (∼8 cm in height) was filled with quartz beads. Before the reaction, the sample was pretreated in the same reactor at 823 K under N_2 flow for 2 h at a 20 mL/min flow rate (the actual reaction temperature was: 803 K). The *n*-hexane/N_2 mixture gas was evenly distributed into the reactor, with W/F = 0.25 (W: amount of catalyst/g, F: feed rate/g h^{-1}). The conversion of *n*-hexane has been regulated by adjusting the W/F ratio by changing the amount of catalyst used. Products were analyzed by online gas chromatographs (Ruimin GC2060, Shanghai), equipped with a flame ionization detector (FID). Rt-QBOND-PLOT capillary columns were connected to the FID for analyzing hydrocarbon products. The product selectivity was calculated on a molar carbon basis.

S2. Supplementary discussion sections

In order to investigate the impact of particle size, the commercially available nano-sized zeolite ZSM-5 was also subjected to catalytic performance evaluation (see **Fig. S12**). Till now, the manuscript file discussed the ZSM-5 zeolite-related results based on micro-sized material (see **Fig. 2-4** in the manuscript). The nano-sized zeolite ZSM-5 was also characterized by analogous techniques, including SEM, ICP-OES, XRD, N_2 physical adsorption-desorption, NH_3-TPD, and ^{27}Al MAS NMR (see **Fig. S11**). The particle size of this material was from tens to hundreds of nanometers with a Si/Al ratio, as determined by ICP-OES, of 16, which is similar to that of micron-sized ZSM-5. The XRD and physisorption characterization displayed patterns usual to nanosized microporous ZSM-5 [**Fig. S11**(b) and (c)]. The NH_3-TPD curve indicates that the catalyst contains both weak and strong acid sites [**Fig. S11**(d)]. This aspect is highly consistent with the relatively higher content of tetrahedral framework Al in its ^{27}Al MAS NMR spectrum [**Fig. S11**(e)]. Next, this nanosized ZSM-5 zeolite catalyst was tested for its catalytic cracking performance on *n*-hexane under the same testing conditions as the micron-sized ZSM-5 (**Fig. S12**). Under the same test conditions as the micron-sized ZSM-5 zeolite catalyst, the conversion rate of *n*-hexane exceeded 60 % with no sign of reasonable deactivation till 30 h. We noticed that the *n*-hexane cracking ability of nanometer-sized ZSM-5 catalyst is stronger than that of micron-sized ZSM-5 (although the conversion was about 20 % higher than that of micron-sized ZSM-5).

S3. Supplementary figures

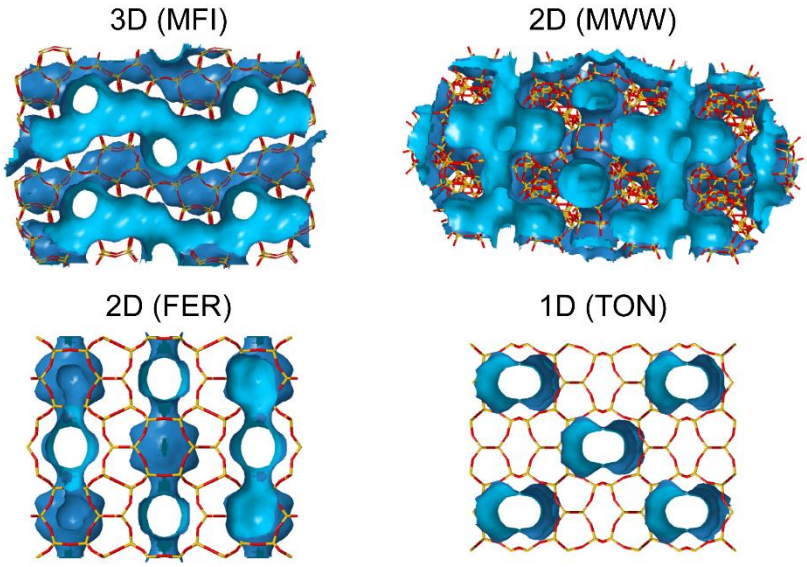

Fig. S1. The schematic diagram of the 3D microstructure of four types of zeolites used in the study.

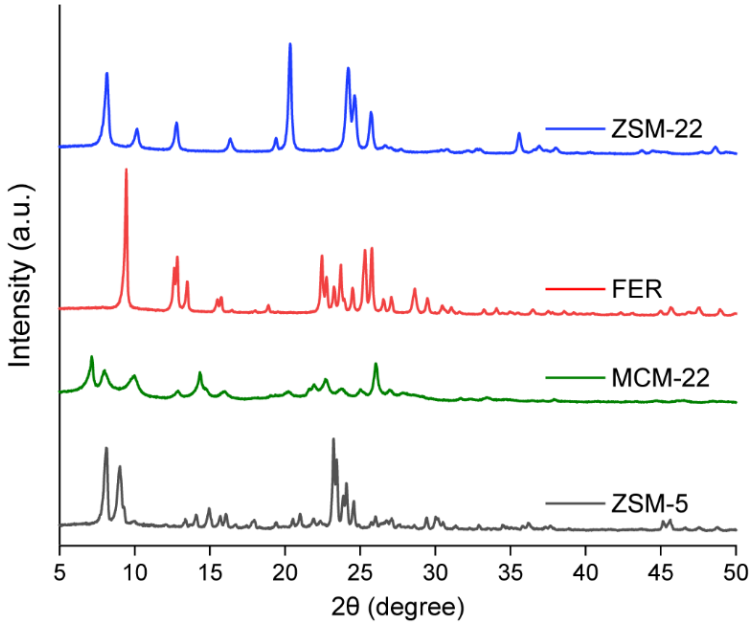

Fig. S2. The powder X-ray diffraction patterns of ZSM-5 (black), MCM-22 (green), FER (red), and ZSM-22 (blue) zeolites. The XRD diffraction peaks of the four commercial zeolites have good consistency and representativeness with the corresponding materials.

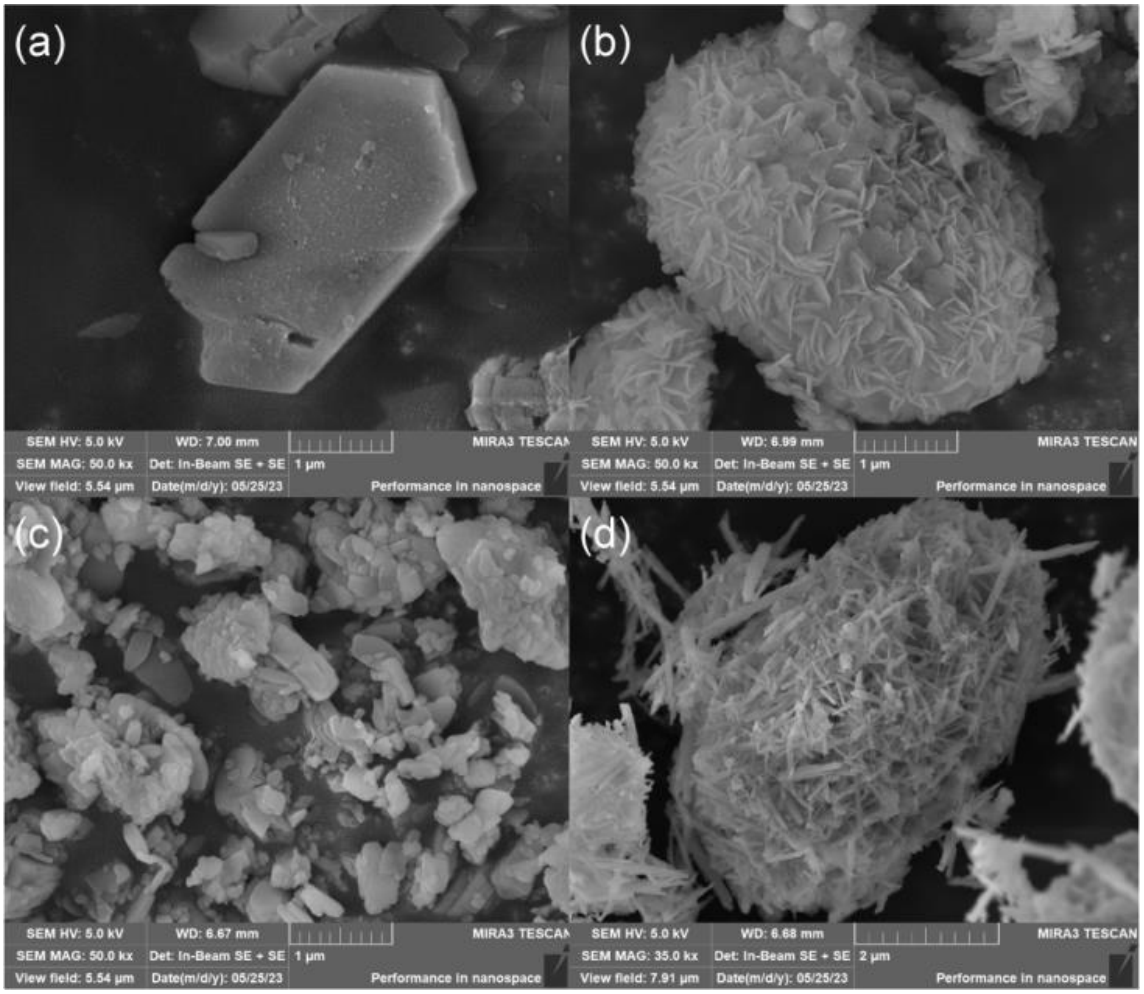

Fig. S3. The representative SEM image of ZSM-5 (a), MCM-22 (b), FER (c), and ZSM-22 (d) zeolites used in this study. ZSM-5 has a typical coffin-like hexagonal prism shape, MCM-22 has a typical petal shaped spherical structure formed by stacking two-dimensional sheet shapes, FER zeolite has irregular shapes, while ZSM-22 has a typical one-dimensional rod-shaped morphology. The crystal size of the four zeolites ranges from a few hundred nanometers to a few micrometers.

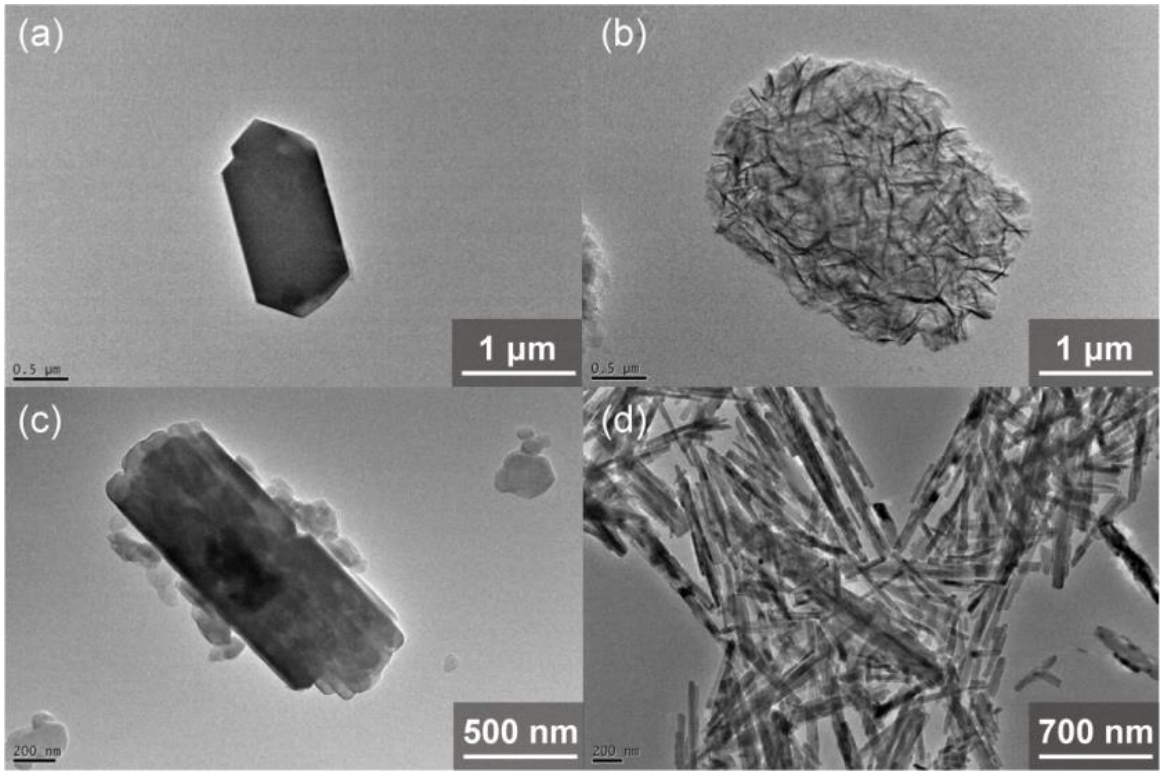

Fig. S4. The representative TEM image of ZSM-5 (a), MCM-22 (b), FER (c), and ZSM-22 (d) zeolites used in this study.

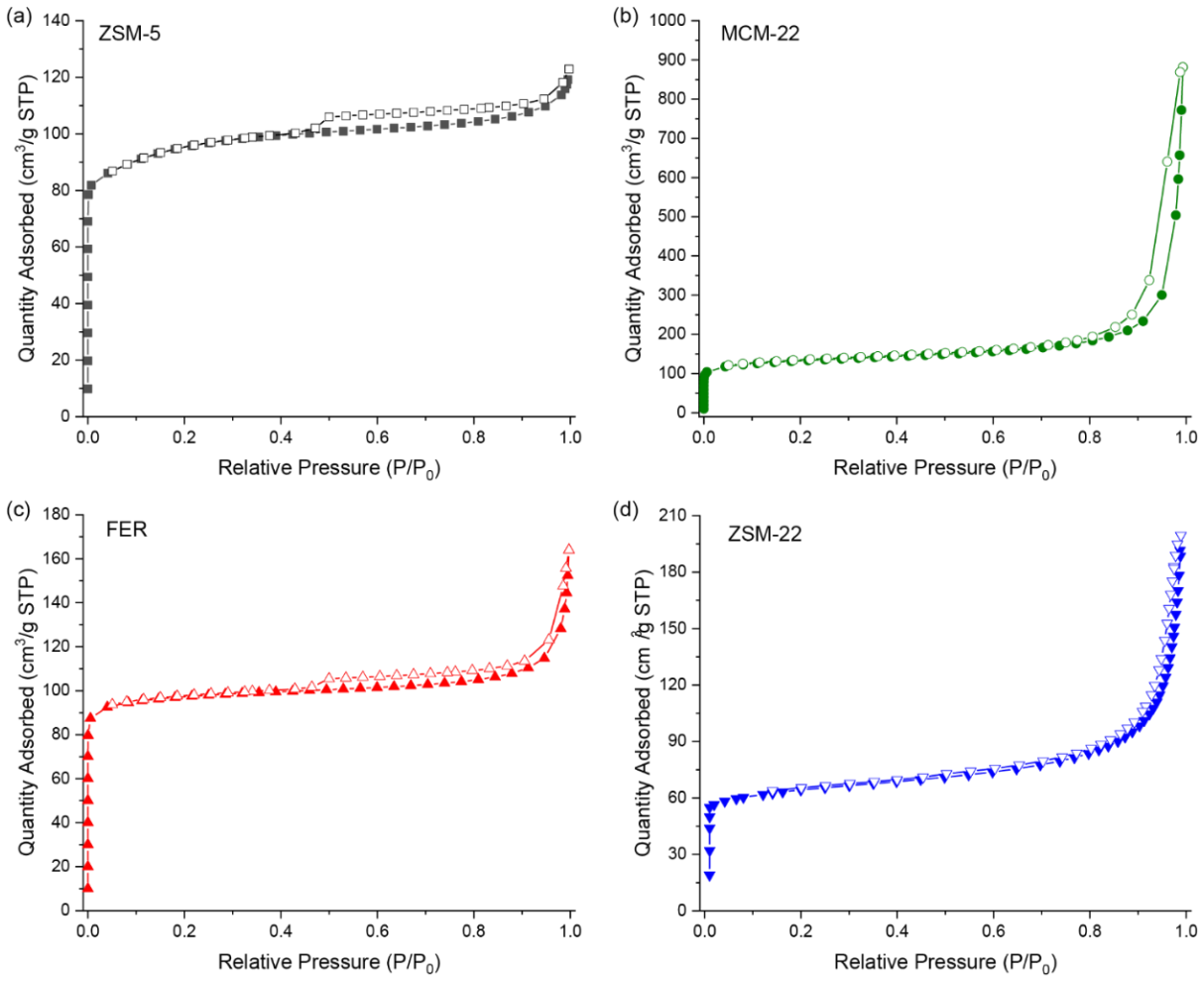

Fig. S5. The N_2 physical adsorption-desorption curves of ZSM-5 (a), MCM-22 (b), FER (c), and ZSM-22 (d) zeolites were used in this study. The N_2 physical adsorption-desorption curves of the four zeolites are typical Type I isotherms, indicating the presence of microporous structures in the zeolites. The return loop of relative pressure (P/P_0) in the range of 0.5-1.0 could be attributed to the interparticle mesopores. See **Table 1** for the physisorption parameters.

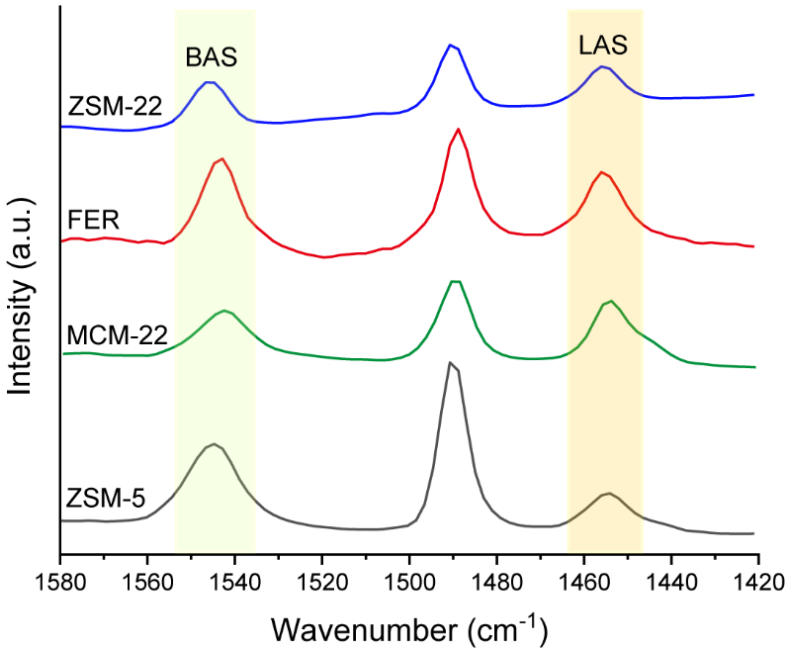

Fig. S6. The Py-FTIR spectra of ZSM-5 (black), MCM-22 (green), FER (red), and ZSM-22 (blue) zeolite samples used in this study were desorbed under vacuum at 423 K for 30 min. The characteristic peaks at 1546 cm^{-1} and 1455 cm^{-1} were typically attributed to Brønsted acid sites (BAS) and Lewis acid sites (LAS) of zeolites, respectively. See **Table 1** for further details.

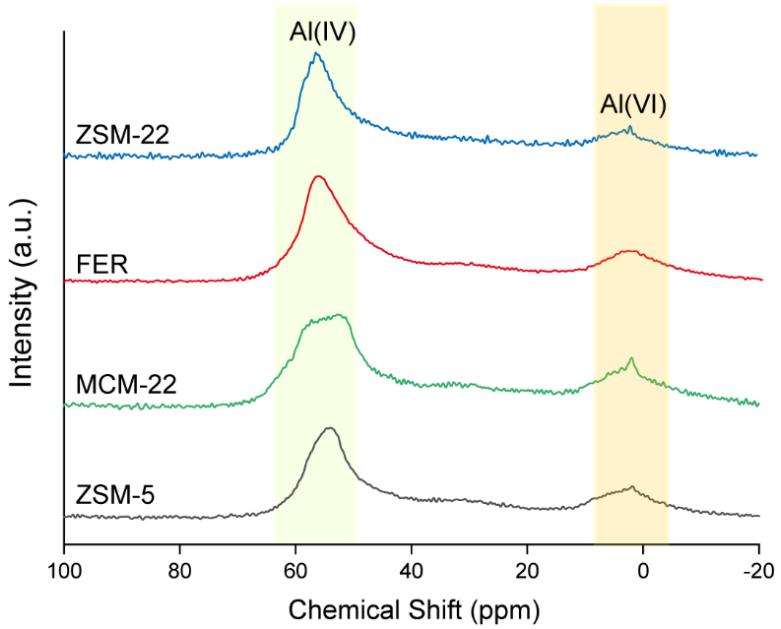

Fig. S7. ^{27}Al MAS solid-state NMR spectra of ZSM-5 (black), MCM-22 (green), FER (red), and ZSM-22 (blue) zeolites used in this study. [magic-angle spinning (MAS) = 15 kHz, number of scans (NS) = 5 k].

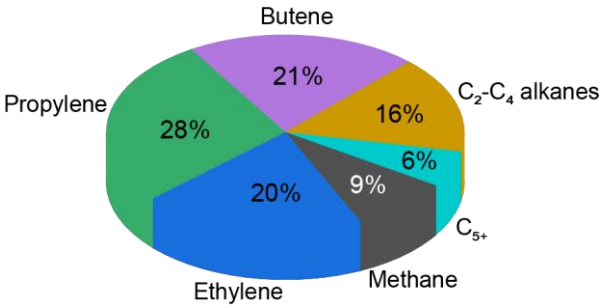

Fig. S8. The product distribution of non-catalytic thermal cracking of *n*-hexane (average conversion of ~ 5.5 %). Reaction conditions: N_2: 40 mL/min, *n*-hexane: 0.02 mL/min, the reaction temperature was 803 K, P = 1 atm. The product selectivity is the average of three sets of experimental data collected within 3 h.

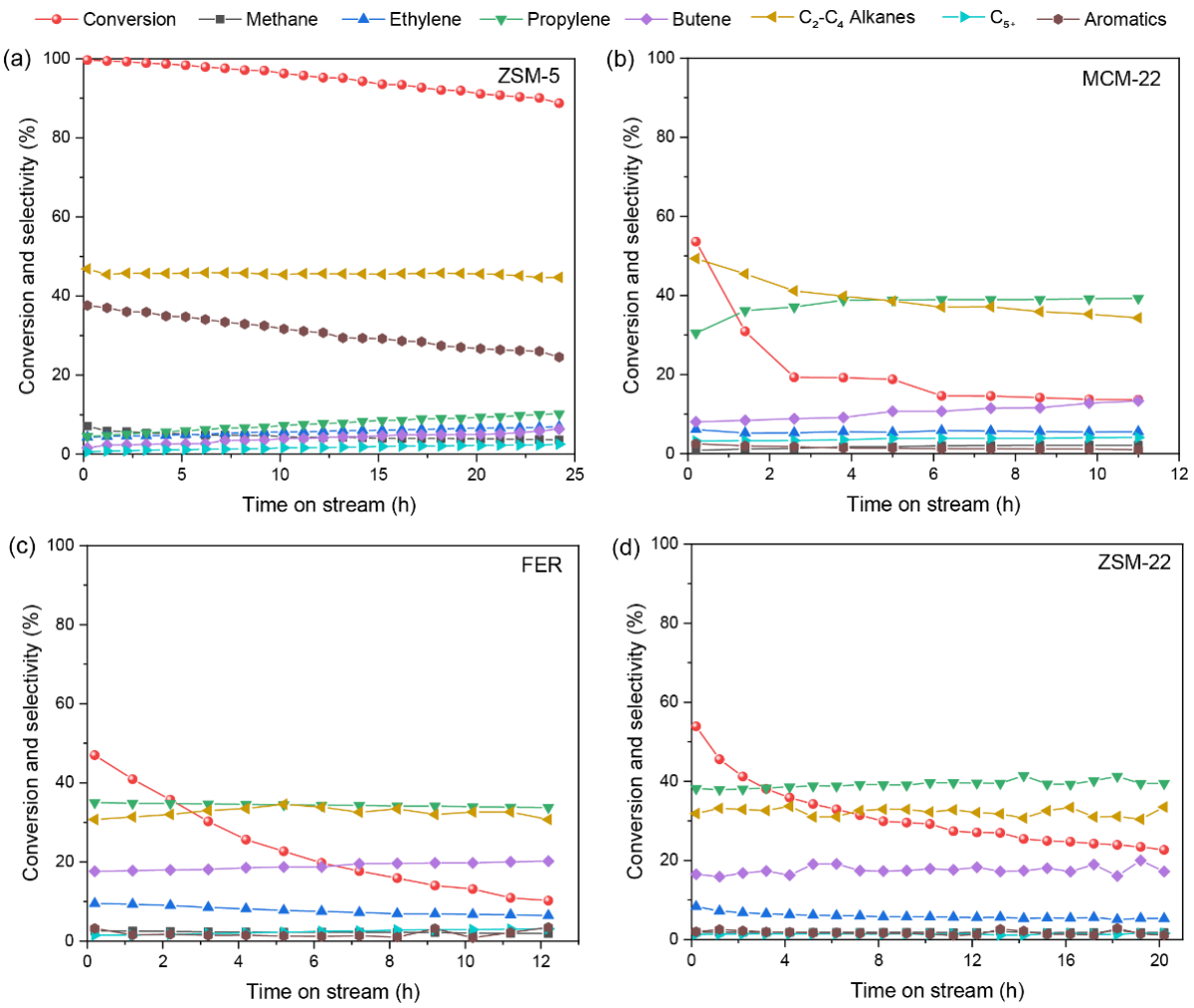

Fig. S9. The catalytic results of *n*-hexane cracking reactions showing the products selectivity in the effluent gas-phase and *n*-hexane conversion as a function of time on stream (TOS) for the following zeolites: (a) ZSM-5, (b) MCM-22, (c) FER, and (d) ZSM-22.

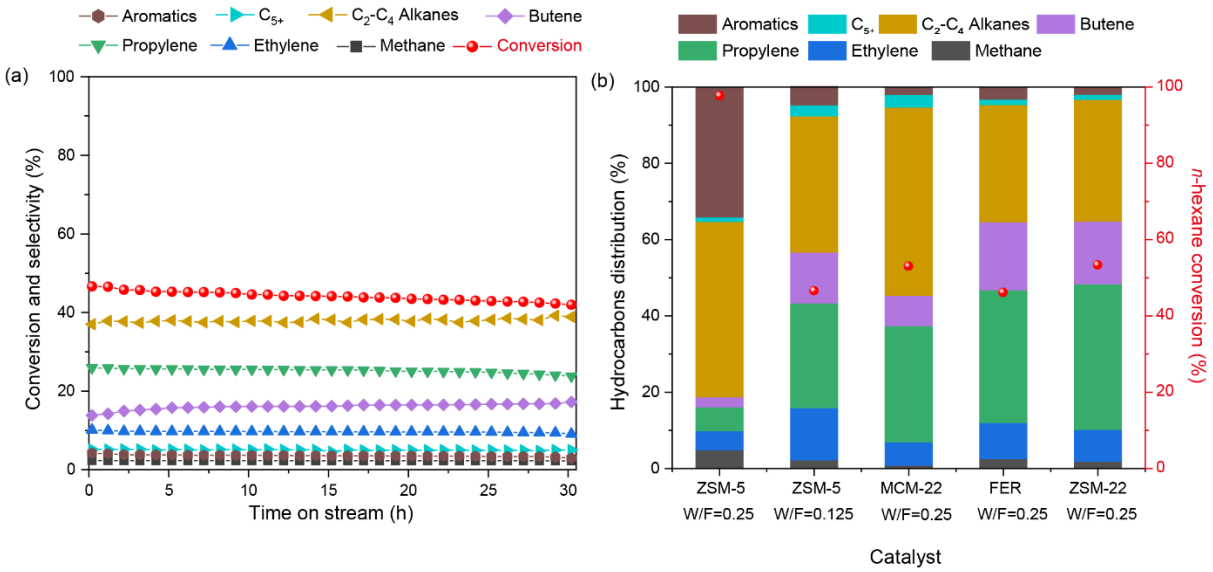

Fig. S10. Additional catalysis data: (a) *n*-hexane catalytic cracking over micron-sized ZSM-5 catalyst to lower the conversion level compared to other zeolites (see **Fig. S9** above) (Reaction conditions: catalyst: 0.1 g, N_2: 40 mL/min, *n*-hexane: 0.02 mL/min, the reaction temperature was 803 K, P = 1 atm, W/F = 0.125). (b) Hydrocarbon distribution in the effluent gas-phase over all zeolites at time-on-stream of ~ 6.2 h. The different colored blocks in the bar chart represent the selectivity of the corresponding products. The red ball mark indicates the corresponding *n*-hexane conversion rate. The corresponding space velocity values are marked below the zeolite names, as follows (left-to-right): micron-sized ZSM-5 (W/F = 0.25, 0.125), MCM-22 (W/F = 0.25), FER (W/F = 0.25), and ZSM-22 (W/F = 0.25).

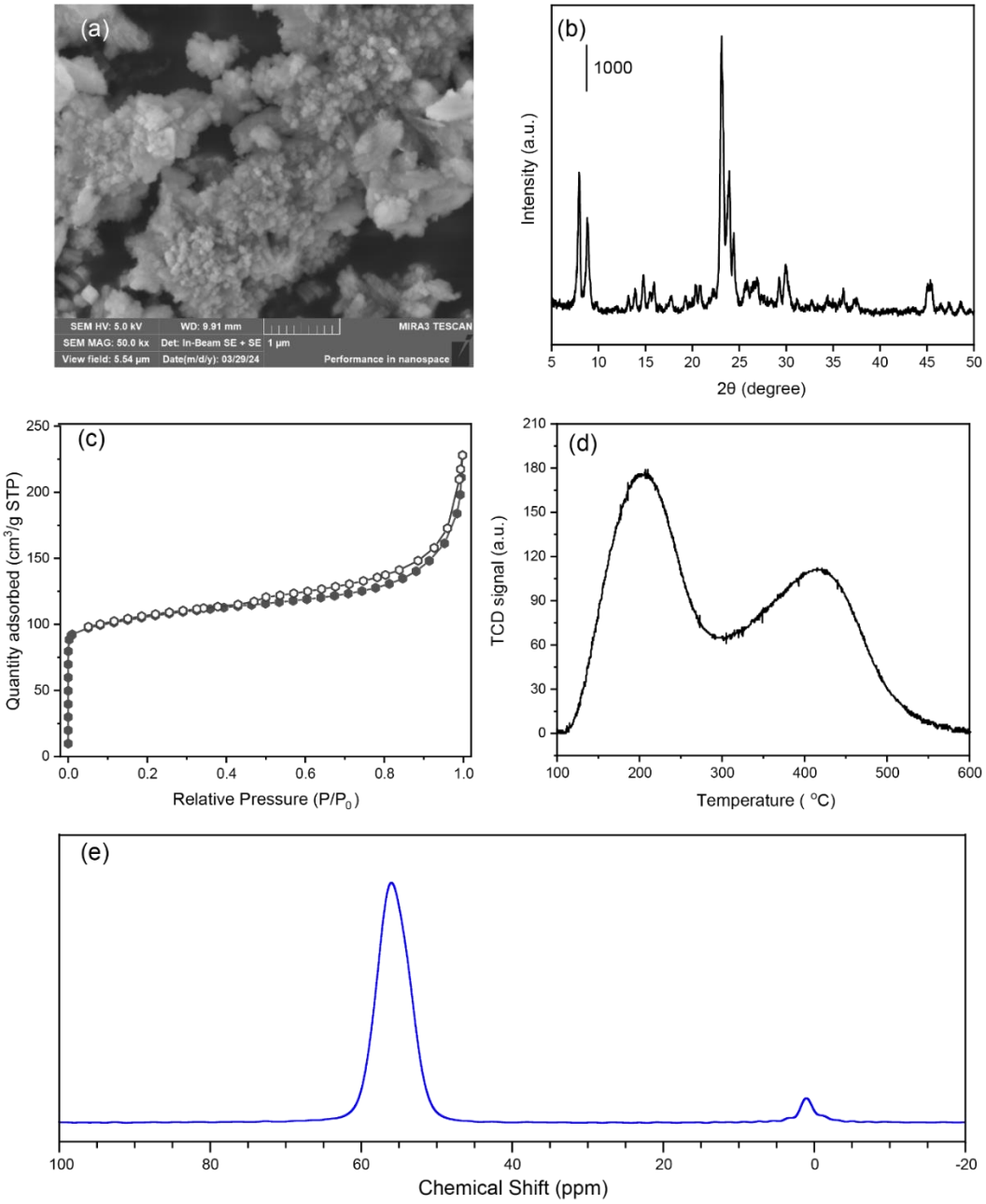

Fig. S11. The additional characterization nanometer-sized ZSM-5 catalyst: (a) SEM, (b) XRD, (c) N_2 physical adsorption-desorption curves, (d) NH_3-TPD, and (e) 1D ^{27}Al MAS NMR. Also see **Fig. S2-S7** for characterization of micro-sized ZSM-5 for the sake of comparison.

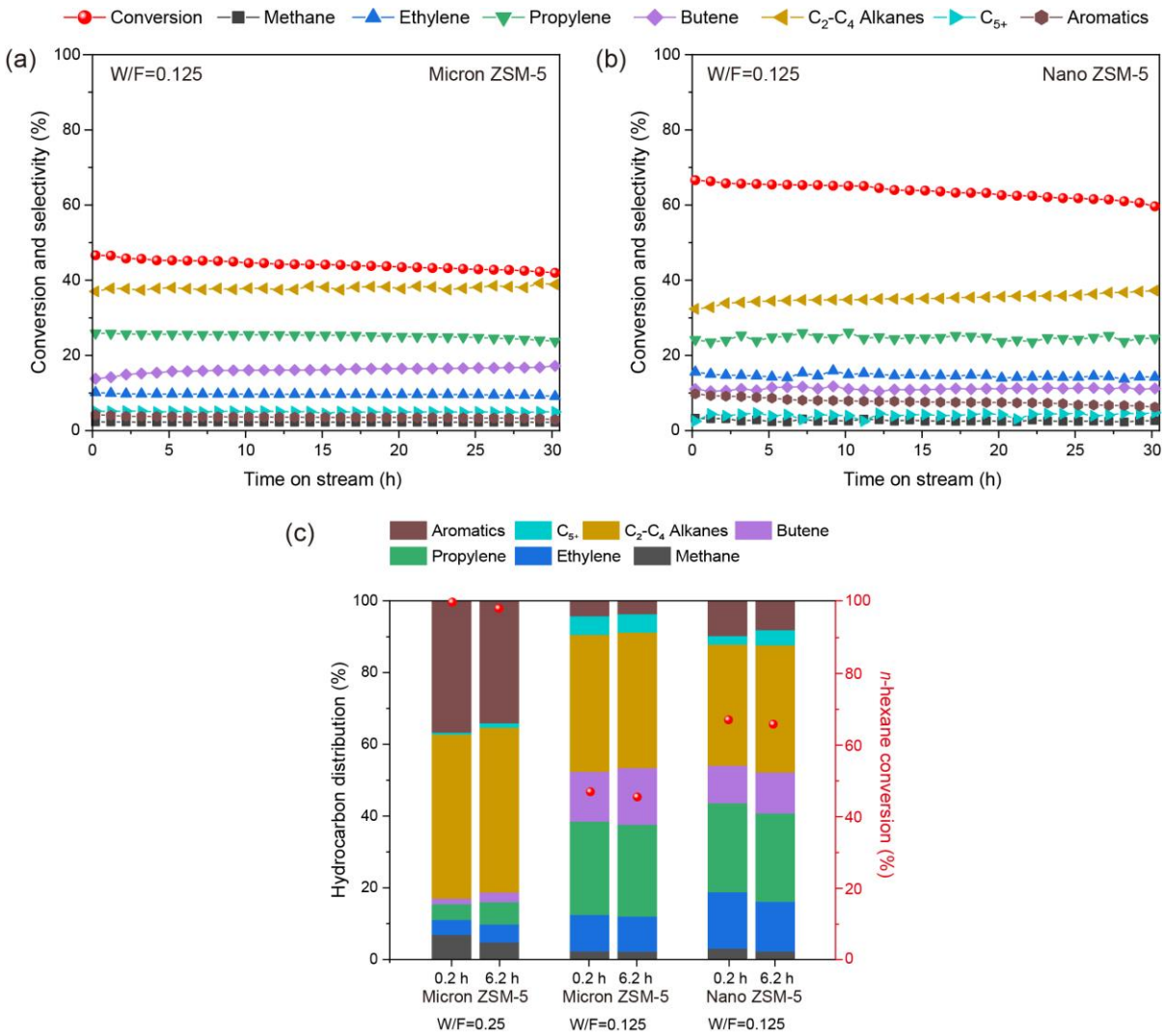

Fig. S12. The catalysis comparison of (a) micro-sized and (b) nano-sized zeolite ZSM-5 during the catalytic cracking of *n*-hexane as well as their (c) comparison on hydrocarbon distribution at time-on-stream of ~ 0.2 h and ~ 6.2 h in the effluent gas-phase. The different colored blocks in the bar chart represent the selectivity of the corresponding products. The red ball mark indicates the corresponding *n*-hexane conversion rate. The corresponding space velocity values are marked below the zeolite names.

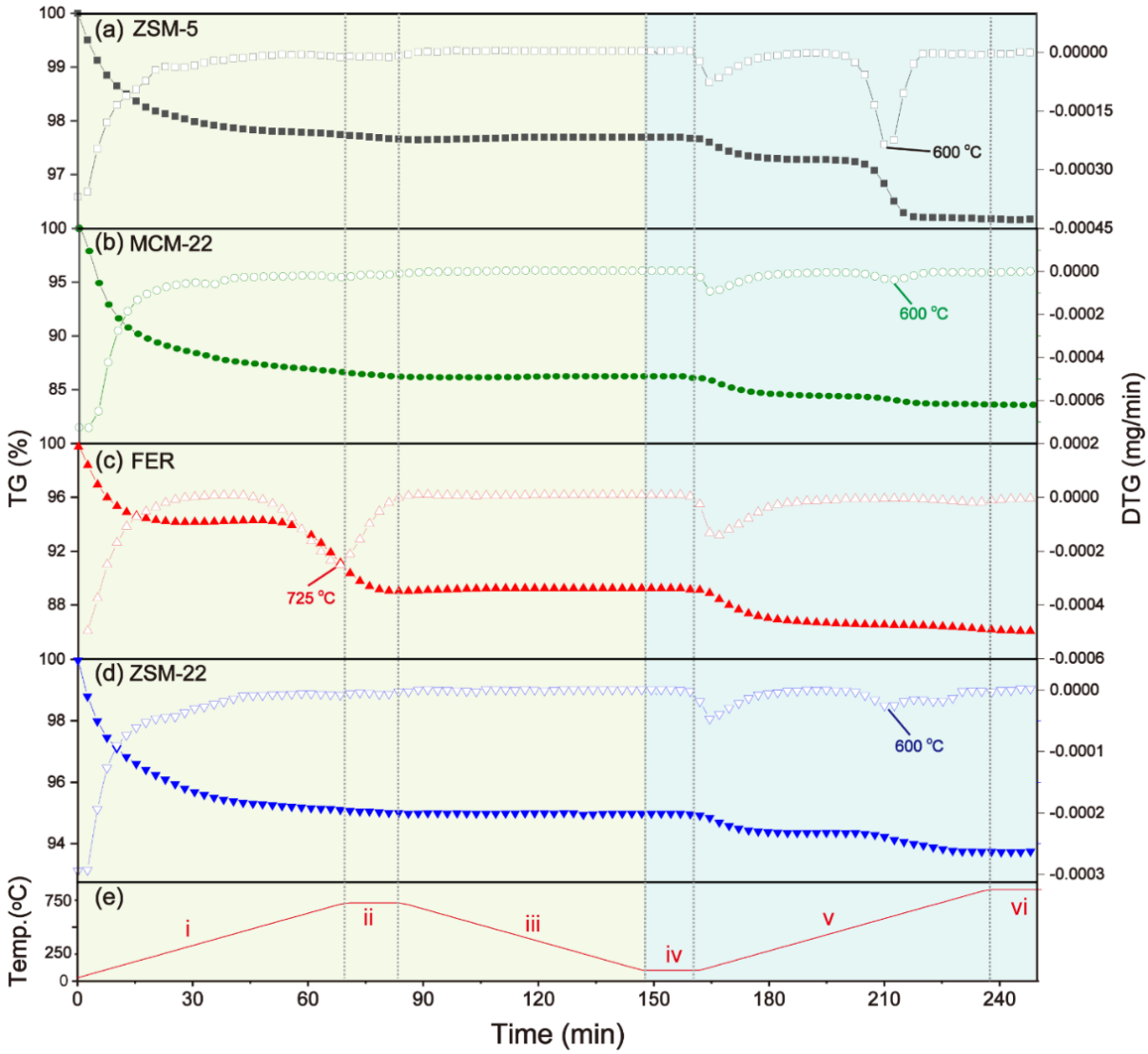

Fig. S13. The TGA/DTG (left zone in light green: tested at N_2 atmosphere to analyze the soft coke and right zone in light cyan: tested at air atmosphere to analyze hard coke) test results of ZSM-5 (a), MCM-22 (b), FER (c) and ZSM-22 (d) zeolite samples after the reaction. The temperature variation curve over time during the program heating process (e). In addition to investigating the catalyst deactivation, these TGA/DTG profiles also help us to study the coke properties of zeolite used in this study and deactivation.

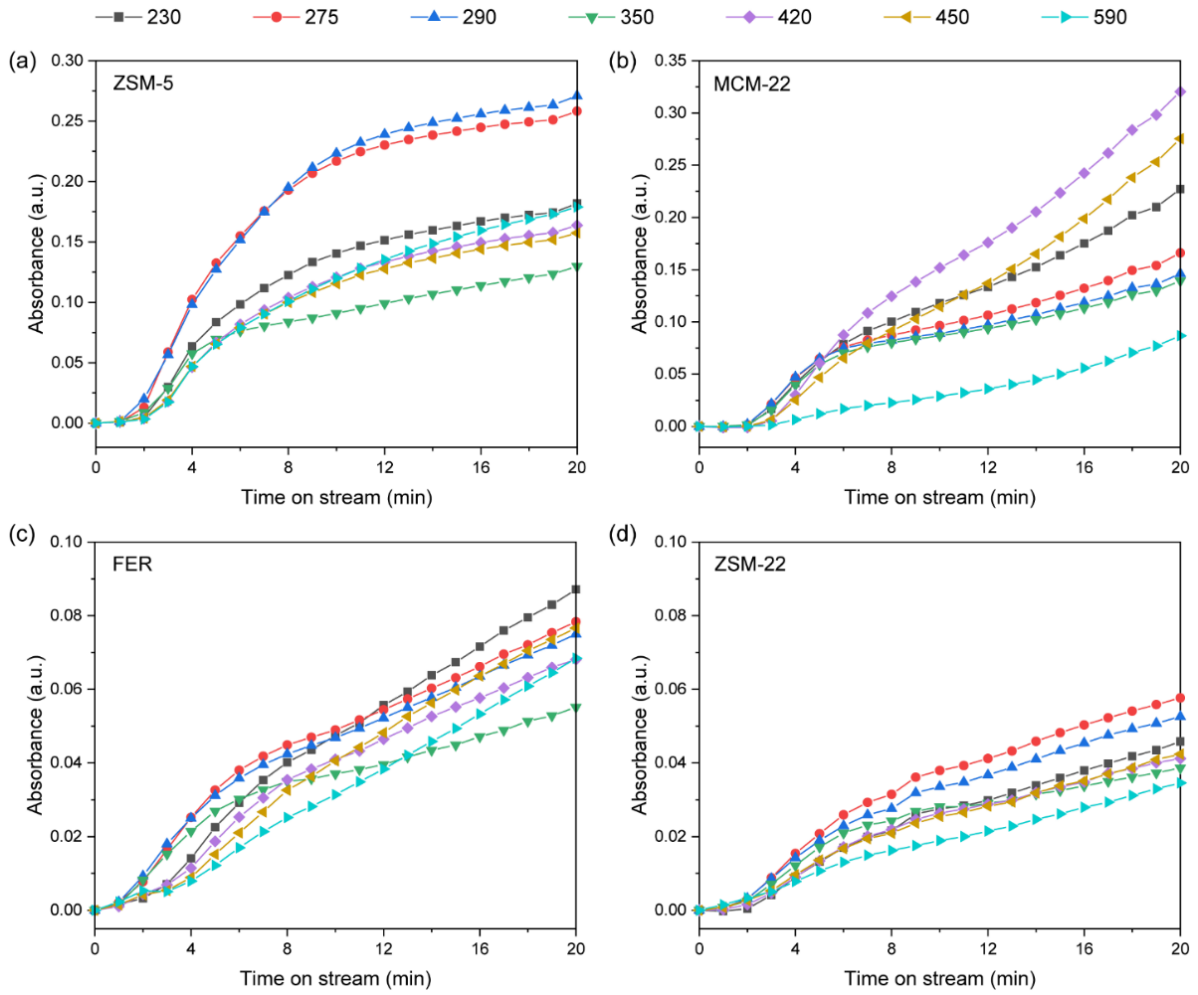

Fig. S14. The key UV-vis bands as a function of time on stream (TOS) for the following zeolites: (a) ZSM-5, (b) MCM-22, (c) FER, and (d) ZSM-22.

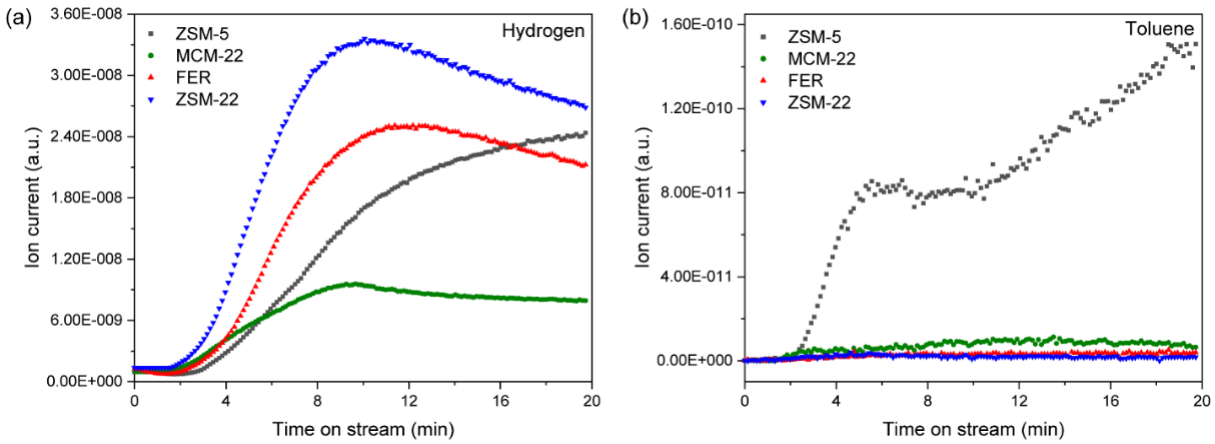

Fig. S15. The overlapping mass-spectra profiles for (a) hydrogen and (b) toluene over ZSM-5 (black), MCM-22 (green), FER (red), and ZSM-22 (blue).

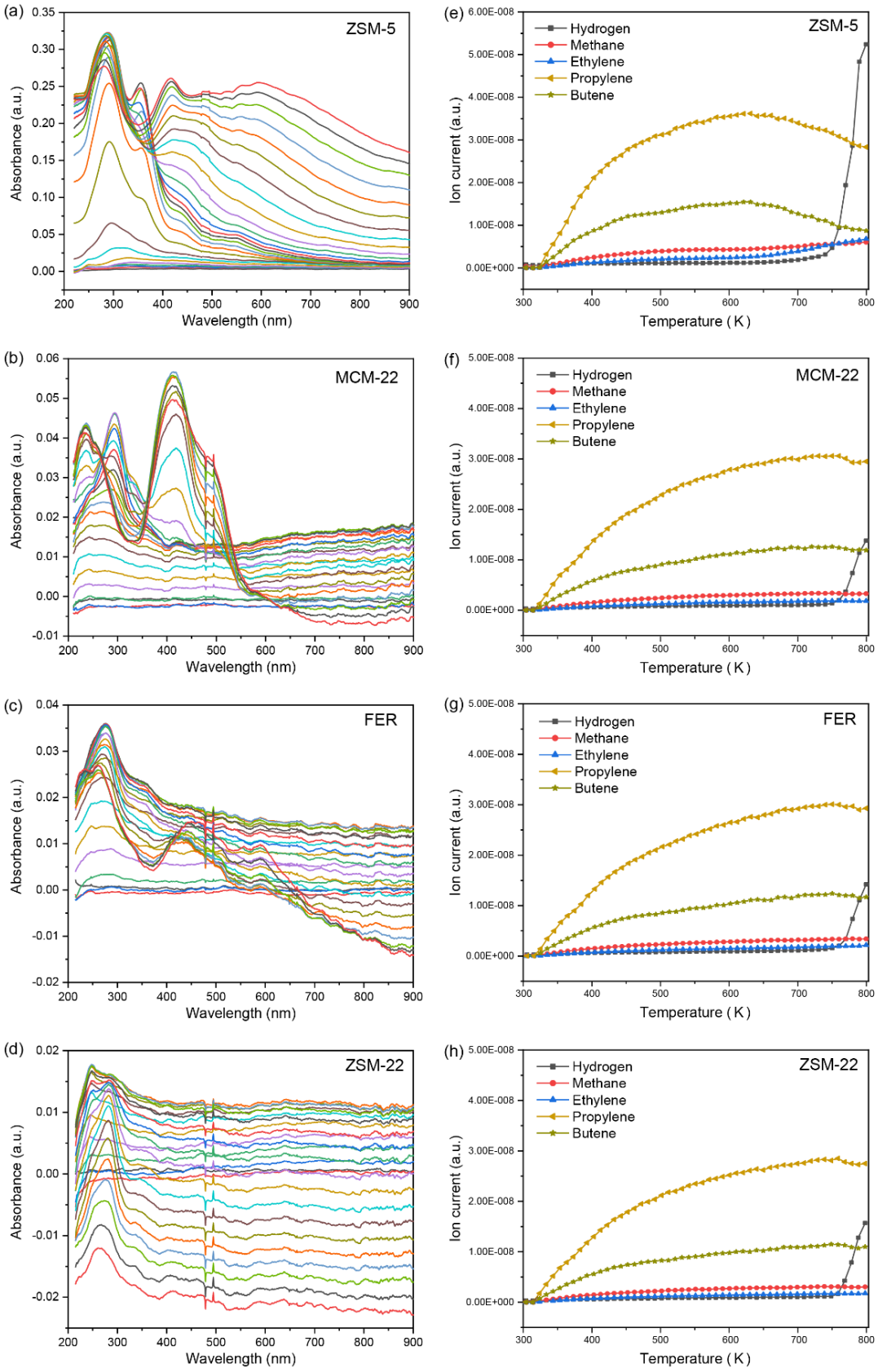

Fig. S16. The *operando* mechanistic study over the chemisorbed zeolite. In this case, the reactant was not continuously flowed through the *operando* cell; rather the reactant was pre-adsorbed over zeolite, which was further subjected to *operando*-like experiments by UV-vis

DRS and MS: (a-d) temperature-monitored UV-vis DRS profile and (e-h) temperature-resolved mass-spectral profiles of key hydrocarbon effluent species during the catalytic *n*-hexane conversion over zeolites ZSM-5 (a, e), MCM-22 (b, f), FER (c, g) and ZSM-22 (d, h). The temperature range is from 303 K to 803 K, with a programmed temperature rise of 10 K/min. We refer to **Fig. 3**, **S14-S15** for the continuous flow *operando* experiments for the sake of comparison.

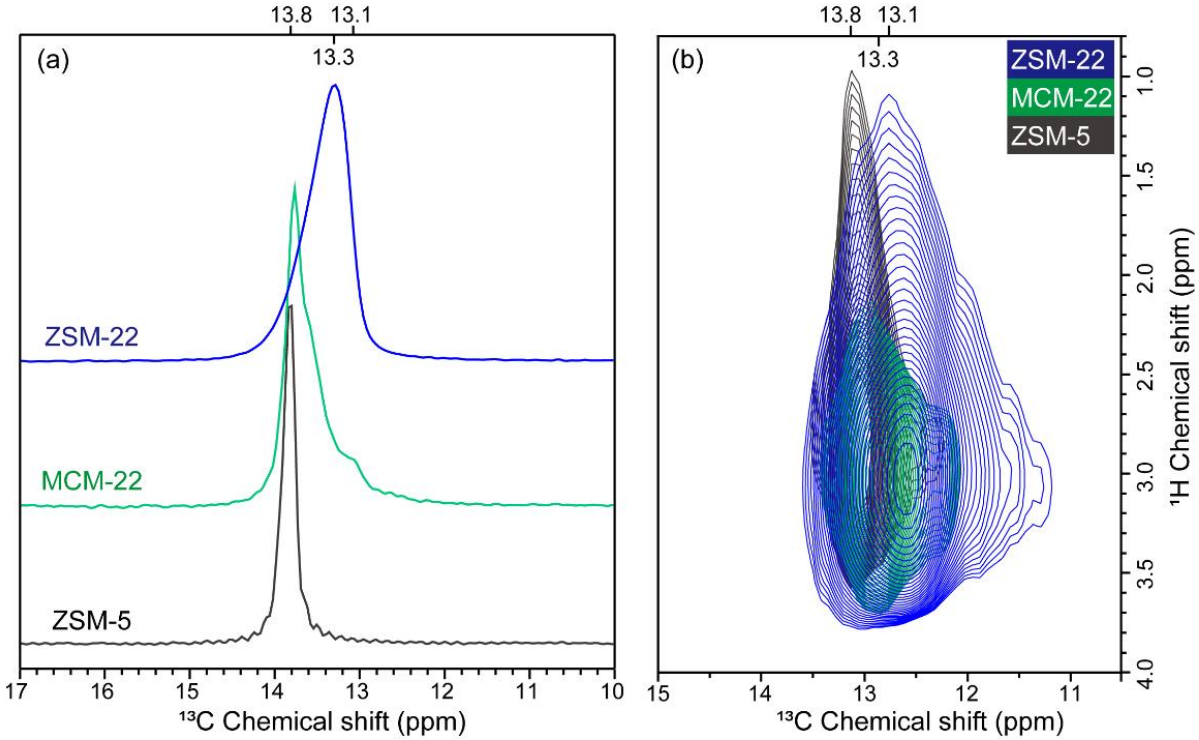

Fig. S17. The partial enlarged view of (a) 1D ^{1}H-^{13}C CP (MAS = 16 kHz) and (b) 2D ^{1}H-^{13}C CP HETCOR MAS NMR spectra of molecules trapped in the zeolites (MAS=10 kHz) after the hexane-1-^{13}C conversion over ZSM-5 (black), MCM-22 (green) and ZSM-22 (blue) for 10 min at 803 K [magic-angle spinning (MAS), cross-polarization (CP)]. The broader peak shape in 1D and elongated signals in 2D NMR indicate the heterogeneity within the micro-environment of zeolites, where the analogous immobilized nature of molecular scaffolds resides in the non-identical environment within the zeolite.

S4. Supplementary References

1 C. A. Emeis, *J. Catal.,* 1993, **141**, 2, 347–354.

2 X. Zhang, H. Zhou, Y. Ye, X. You, X. Zhou, S. Jiang, K. Liu and A. Dutta Chowdhury, *Inorg. Chem. Front.,* 2023, **10**, 6632–6645.

3 G. Kresse and J. Furthmüller, *Comput. Mater. Sci,* 1996, **6**, 15–50.

4 G. Kresse and J. Hafner, *Phys. Rev. B,* 1994, **49**, 14251–14269.

5 J. P. Perdew, K. Burke and M. Ernzerhof, *Phys. Rev. Lett.,* 1996, **77**, 3865–3868.

6 S. Grimme, J. Antony, S. Ehrlich and H. Krieg, *J. Chem. Phys.,* 2010, **132**, 154104.

7 D. Joubert, *Phys. Rev. B Condens. Matter Mater. Phys.,* 1999, **59**, 1758–1775.

8 A. Ramirez, X. Gong, M. Caglayan, S. A. F. Nastase, E. Abou-Hamad, L. Gevers, L. Cavallo, A. Dutta Chowdhury and J. Gascon, *Nat. Commun.,* 2021, **12**, 5914.

9 T. Li, S.-H. Chung, S. Nastase, A. Galilea, Y. Wang, I. Mukhambetov, M. Zaarour, J. C. Navarro de Miguel, J. Cazemier, A. Dokania, L. Panarone, J. Gascon, L. Cavallo and J. Ruiz-Martínez, *Chem Catalysis,* 2023, **3**, 100540.

10 S. A. F. Nastase, A. J. O'Malley, C. R. A. Catlow and A. J. Logsdail, *Phys. Chem. Chem. Phys.,* 2019, **21**, 2639–2650.

11 S. A. F. Nastase, C. R. A. Catlow and A. J. Logsdail, *Phys. Chem. Chem. Phys.,* 2021, **23**, 2088–2096.